20

MICROSCOPY

Mariamne Dehonor, Carlos López-Barrón, and Christopher W. Macosko

20.1 INTRODUCTION

Polymer and polymer-related materials are characterized by scanning electron microscopy (SEM), transmission electron microscopy (TEM), scanning transmission electron microscopy (STEM), high resolution transmission electron microscopy (HRTEM), energy-dispersive X-ray (EDX) analysis, electron diffraction energy-loss spectroscopy (EELS), and energy-filtered transmission electron microscopy (EFTEM), among others. The information that these techniques provide is related to the structure, morphology, topology, structure, elemental composition, and chemical bonding of the materials.

This chapter includes a review of the recent literature on polymer microscopy. The basic principles and current challenges of the techniques, as well as the experimental aspects of sample preparation and observation are reviewed elsewhere [1–8]. Specific techniques are surveyed in other reviews; for instance: TEM [9], SEM [10], Field emission SEM [11], and high angle annular dark field (HAADF)-STEM [12].

20.2 TRANSMISSION ELECTRON MICROSCOPY

The characterization of materials using TEM can give information about their structure and morphology. Allied techniques from TEM, such as EDX, EELS, EFTEM, and electron diffraction (ED), can complement the information obtained for a specific material. Several reviews and compilations of the studies on TEM and related techniques are available [13]. In this chapter, some of the most recent applications of TEM and allied techniques to polymer materials have been compiled from 2000 to the present. The focus is on nonconventional techniques such as electron holography, *in situ* TEM, STEM, EELS, cryo-TEM, Z-contrast, etc. In addition, a very detailed section is devoted to 3D imaging.

20.2.1 Conventional Transmission Electron Microscopy

There are several applications of conventional transmission electron microscopy (CTEM), including study of the morphology of polymers and their crystallization behavior. Some reports include studies on the branched crystal morphology of linear polyethylene [14]; the morphology of nucleation and crystallization of polyethylene/carbon nanotubes composites, making evident the behavior of carbon nanotubes as nucleating agents [15]; and the formation of supramolecular polymeric systems as well as the effect of polymer rigidity and the reversibility of self-assembly processes [16].

HRTEM has also been used in the study of polymer crystallinity. A high resolution image is an interference image of the transmitted and diffracted beams. It has been reported that changes in weight-average molecular weight lead to structural changes [17].

Some of the observed changes are related to lamellar thicknesses, disorder in the crystalline packaging of the chains, interconnectivity between crystalline lamellae, as well as tilt angles of the polymer chains.

20.2.2 Transmission Electron Microscopy Allied Techniques

20.2.2.1 Electron Holography

Electron holography is an imaging technique that records the interference pattern of an object on a film or detector, forming a hologram [18]. Electron holography was invented by Dennis Garbor in 1948. He developed the technique to improve the resolution of electron microscopes, by solving the spherical aberration problem of the primary lens that affects the phase components of the electron beam. The method is based on the combination of two waves in the electron microscope, namely, the image wave and the undeviated wave. If the electron optical geometry is correctly set up, these two waves can be made to interfere. The interference pattern would then be processed using optical techniques to form optical holograms. The hologram is a Fresnel diffraction image of the object [2]. Several electron optical geometries have been developed to produce holograms; among them electron holography is an inline scheme and high energy electron holography is an off-axis scheme [19]. Detailed description of both modes can be found elsewhere [20, 21]. In this technique, the phase image can be referred to the variations in the sample thickness due to the change in phase of the electron wavefront in comparison with the original wave. Phase contrast can be carried out by an imaging defocus or by the off-axis holography.

Electron holography is used in several applications, such as in biological samples, for example, bacterial surfaces [22]; in nanocrystals of metallic catalyzers to determine the shapes from the 3D structure and to extract details from the structure and morphology on an atomic scale; in thin films to study electrical and magnetic fields, as magnetic and electric fields can shift the phase of the interfering wave passing through the sample [23]; in ferroelectric materials to enhance contrast between regions of different polarizations [24]; in semiconductor devices [25]; and in polymer nanoparticles to give phase-contrast imaging to avoid the use of a staining procedure [26]. Even though there are many applications using electron holography in materials characterization, only a limited number of scientific reports are found in the polymer field. Specific materials characterized by electron holographic techniques include arborescent graft polystyrene (PS) nanoparticles [26]. Chou et al. [26] have reported that electron holography could provide higher contrast than generated by the traditional method of transferring information to amplitude via defocusing. Electron holography is thus capable of recovering significant phase contrast from the PS particles despite the fact that they provide negligible amplitude contrast. This technique has the advantage of avoiding heavy element staining that induces amplitude contrast but has difficulties in the preparation the analysis of the structures at the nanometer scale.

Polymers are being used as holographic recording material, as reported by Lawrence et al. [27]. According to the authors, photopolymers present several advantages such as ease of production and high efficiencies, even though they have low ability to record high spatial frequency gratings compared to dichromated gelatin and silver halide photographic emulsions. In the same way, Garcia et al. [28] have studied a photopolymer based on acrylamides, consisting of acrylamide as monomer, yellowish eosin as sensitizer, and triethanolamine as radical generator, all on a matrix of poly(vinyl alcohol).

Gölzhäuser et al. [29] studied the optimal conditions (electron energy, width of the electron beam, and the detector size) for low electron point source microscopy using holograms of phthalocyaninato polysiloxane (PcPS), a rodlike macromolecule.

Binh et al. [30] have reported the electron holography of carbon and polymer fibers.

20.2.2.2 In situ Transmission Electron Microscopy

Nowadays, electron microscopy has evolved to allow the determination of polymer morphology and composition to be mapped as a function of time in several physical conditions. In particular, *in situ* microscopy can provide morphological structure and also information on the dynamic changes in properties present in microstructures during synthesis, phase transformations, and physical tests [31].

In general, *in situ* microscopy can be performed by using SEM, TEM, and atomic force microscopy (AFM). By using SEM and environmental scanning electron microscopy (ESEM) techniques, several studies on the deformation, crack propagation, and fracture processes can be carried out. In addition, TEM enables the study of the same processes but at the nanoscale. Finally, AFM images give information about the micromechanical deformation at atmospheric pressure and in the absence of electron irradiation. In general, in addition to mechanical studies, the *in situ* techniques that can be performed over materials using microscopy techniques are heating and cooling, electron irradiation, application of electric and magnetic fields, and application of different ambient atmospheres, among others [2]. It is also common to use a combination of *in situ* techniques, such as deformation tests using temperature variations. In all cases, microscopy images can be observed in real time but the sample preparation varies depending on the technique.

In situ TEM can be performed to study the optical, electrical, and mechanical properties of materials. The instrumentation involved considers several types of specimen holders. At present, the main types of specimen probes used in industry are electrical probing (TEM–STM) [32], micro-force (TEM–nanoindenter) [33], nano-force (TEM–AFM) [34, 35], optical, scanning fiber, multiple electrical wire,

and some of their combinations [36–39]. In all cases, very thin samples (100–500 nm) are required.

In general, the applications of *in situ* TEM involve the understanding of the relationship between the physical properties and the structure of nanomaterials.

In addition to the electrical and mechanical properties that can be directly extrapolated from macro-sized experiments, it has been reported that it is possible to bring optical signals into TEM and position them on selected areas of the specimen using an external laser beam, or to acquire optical emission from a specimen to analyze it externally. Regarding external laser illumination with simultaneous TEM imaging, the reported applications are (i) sintering of powder specimens; (ii) heating to induce phase or structural changes in specimens; (iii) illumination of photovoltaic specimens with simultaneous electrical current measurement; and (iv) illumination of photocatalytic materials with simultaneous electrical current measurement. The applications that involve acquiring emitted light from specimens include (i) cathodoluminescence used to investigate photonic materials and (ii) temperature determination.

Heating of specimens followed by the study of changes in TEM images allows the observation of phase transformation, alloying, sintering, element diffusion, grain size changes, defect motion, etc.

Specific reports on the applications of *in situ* TEM in polymer materials are described in the following paragraphs.

Synthesis Crozier et al. [40] have reported the gas-phase polymerization of polypropylene using Ziegler–Natta catalysis performed in an *in situ* environmental TEM. In this case, the monomer was introduced into the microscope and the probability of polymerization when the monomer strikes an active site was calculated using the available area of the catalyst.

Crystal Morphology Crystal morphology determines the mechanical properties, the biodegradability, and the biocompatibility of polymers. Thus, it is necessary to understand the mechanism of polymer crystallization in order to control the polymer microstructure and, thereby, its properties. The crystallinity and cavitation of polymers have been studied using optical and *in situ* electron microscopy as complementary techniques, among many others.

Mechanical Strength Stress measurements can be conducted using SEM and TEM. A report on the mechanical properties of polyethylene under deformation and fracture was presented [41]. Three types of fractures depending on the molecular weight and linearity, namely, crazing, elongation, and the "interfacial splitting" of spherulites were described.

It is well known that the main mechanisms of inelastic deformation are shear yielding and multiple crazing in the rigid matrix phase, as well as cavitation in the soft dispersed phase in rubber-toughened plastics and multiphase polymers [42]. For many years, these mechanisms have been studied using microscopy techniques.

Garcia Gutierrez et al. [43] studied the crazing behavior of linear and long-chain branched polystyrene (PS) as function of temperature. The changes of temperature around the glass-transition temperature favor the disentanglement that consequently modifies the characteristics of the crazes (in this case from homogeneous to fibrillated). Using this technique, the deformation rate could also be analyzed.

Rubber-modified amorphous polymers and butadiene-styrene block copolymers have been observed to enhance the plastic yielding of the amorphous glassy components PS and poly(methyl methacrylate) (PMMA). These materials were analyzed using deformed samples or by *in situ* deformation tests of thin sections using TEM and scanning force microscopy (SFM) [44]. Toughening studies in rubber-modified polymers have been performed by Michler and Bucknall [45]. Their experiments on the deformation mechanisms in various rubber-modified polymers were carried out using microscopy techniques. From these studies, two new mechanisms of energy absorption were found. In particular, *in situ* mechanical tests were carried out using *in situ* TEM.

Studies from the composite deformation mechanism and interfacial bonding between nanofillers and the polymer matrix have been performed [46–48]. In these reports, the authors performed straining studies to determine the load transfer between carbon nanotubes and the polymer and observed the phenomena of crack propagation and polymer debonding. In some cases, the mechanical deformation processes were followed over the electrospun composite fibers. Microscopic images revealed information on the dispersion and orientation of nanotubes within the fiber and their impact in the mechanical performance regarding strain at break and stress concentration at the pores of the nanotubes.

Other types of nanocomposites have been studied, such as PMMA/montmorillonite [49]. In this system, tensile tests were performed using TEM to obtain information on the deformation process.

Processing Polymer processing properties that affect the crystallization stages can be studied in detail using *in situ* probes. Several reports on this application have been published. Among them, the rheology of polyethylene and polyethylene blends was studied by *ex situ* TEM to determine their crystallization process and its effect on the shear behavior. The obtained information at different length scales (during shear flow and flow during crystallization) was used to construct a crystallization process model [50].

The relationship between shear history and the subsequent anisotropic crystal growth is of particular interest.

Additional applications of *in situ* TEM include *in situ* measurement of the interfacial adhesive forces in nanoparticles and biological samples [51].

20.2.2.3 *Scanning Transmission Electron Microscopy*

STEM is a type of TEM. In this type of microscopy, the electron beam is focused to a narrow spot, which is scanned over the sample. The scanned electrons traverse the samples as in CTEM. Using this technique, several analyses such as mapping by EDX spectroscopy, EELS, and annular dark-field (ADF) imaging can be performed. Both types of information, image and quantitative data, can be obtained. It is noteworthy that STEM imaging provides information from a volume of the material, and therefore in the case of films, it provides information on the membrane thickness [49].

Biological Samples Some studies of biological architectures from tissues and cells have been performed by combining confocal light microscopy, TEM, STEM, and focused ion beam (FIB). The images from the STEM technique were used to explore the morphology of the materials as 3D relationships for a range of length scales and materials [52].

Specific examples using STEM include structural studies over chitin gels used to produce chitin films. The results of the tests performed revealed that shrinkage resulted in a coarser microstructure. This morphology affected the tensile properties. It was also observed that shrinkage was proportional to the ductility and roughness of the meterial [53].

Polymers Regarding polymer particulate systems, it has been reported that SEM has been employed to examine particle size and shape, and STEM has been used to characterize the internal structure of multilayer particles [54]. Thus, it was possible to follow the synthesis of particles by STEM. In fact, particles from different morphologies have been studied by several groups.

Particles from polyisoprene (PI) and PMMA were prepared in solution. The obtained lamella-structured block copolymer particles and their cross-sectional images were observed by a staining procedure using STEM [55]. The authors reported that the lamellar phase changed to disordered structures when the suspension of nanoparticles was annealed. In addition, they followed the particle versus the planar film stability.

Polymer particles have been observed using STEM in order to find the differences in their internal structures. Examples include particles of poly(styrene-*b*-sodium acrylate), poly(styrene-*b*-4-vinylpyridine), and poly(styrene-*b*-isoprene) prepared by solvent evaporation [56]. In these systems, the differences between amphiphilic (hollow

structures) and hydrophobic block copolymer nanoparticles (lamellar microphase separation structures) were analyzed. Poly(styrene-*ran*-styrenesulfonate) (P(S-SS$_x$)) ionomers have also been analyzed [57, 58].

A latex used for coating applications and made from an acrylic phase and an alkyd phase contains surfactant particles that stabilize the phases after the film-forming process. Using STEM, the imaging of these surfactant molecules was carried out in order to understand the influence of the surfactant–polymer affinity on the surfactant location after film formation [59].

The grafting process of polymer chains over particles or fibers can be analyzed using STEM, among other techniques. The aspects that can be studied by STEM are the distribution of the polymer chains obtained at different particle/fiber concentrations and the effect of the surface rugosity and composition on the distribution of the polymer, among others [14]. Other examples involving polymeric chains grafted on macroporous silica gel were analyzed using a procedure involved staining, embedding in epoxy, and ultrathin slicing [58].

The synthesis of carbon nanotubes with metal hybrids has been studied using STEM and ED. The carbon nanotubes could be functionalized (or not) with a polymer. Gao et al. [60] have reported particle sizes of 2–20 nm and a metal deposition of 82 wt%.

Additional applications of STEM include (i) the imaging of multilayer particles, considering PS and poly(trifluoroethyl methacrylate) (PTFEMA) particles [54], as well as the distribution of polymer layers covalently grafted on the inner and outer surfaces of macroporous silica gel particles; (ii) the nucleation of spherulites in crystalline and semicrystalline polymers filled with particles, observing that the nucleating efficiency of the filler depends on the size and on the crystallographic orientation of the facet [61]; (iii) the miscibility of polymers in a blend as a way to observe the interface of materials [62]; (iv) the penetration (diffusion) of poly(ethylene glycol) (PEG) chains into wood cell walls [63]; (v) the morphologies of cured epoxy/brominated-phenoxy blends [64]; and (vi) the confirmed presence of quantum dots of (CdSe)ZnS surrounded by protein oligomers [65].

Polymer Nanocomposites The morphology and dispersion state of a filler-like sepiolite (lamella and fiber type) were determined using STEM [66].

Some improvements in the analysis of the morphology by STEM have been reported. In one study, the authors used the deconvolution of the ionomer images by the Pixon method with a simulated electron probe in order to enhance the overall image quality and the detection of subnanometer-scale features (in size and shape) compared to the original ones. The use of deconvoluted images instead of the original ones makes it possible to follow the

distribution of ions in the aggregate, discriminating over-lapping particles. Studies of ionic aggregate distributions have been reported in polymer matrix systems [67, 68].

20.2.2.4 Wet-STEM

Gai [69] proposed in 2002 the development of wet environmental scanning transmission electron microscopy (wet-ESTEM) experiments in order to perform direct probing of controlled liquid–catalyst reactions. The first nanoscale images from dynamic liquid hydrogenation and polymerization reactions of polyamides were then reported.

Furthermore, Bogner et al. [70] proposed experiments using a STEM imaging system to make transmission observations of wet samples in an ESEM without poor contrast or drifting of objects, as obtained in the ESEM of particles that are embedded in a liquid medium. The proposed system was based on ADF imaging conditions and considers specific features to allow slow-scan, high definition imaging of particles below tens of nanometers. The applications of wet-STEM include the studies of emulsion samples of latex polymer-grafted particles [70], polymer-grafted natural rubber particles [71], and clay platelets [72], among others. In several cases, the images acquired showed good resolution and contrast, without staining. In particular, Wet-STEM images provide important information about grafted particles in their native state in solution. Additional applications involve solution-solid and solution-gas-solid reactions in the chemical and biological sciences, as well as thin polymer and biological films.

Theoretical studies of this technique were carried out by Barkay [73]. In this study, wettability (aqueous nanodroplet shape and contact angle) at the nanoscale was quantified using Monte Carlo simulation. The technique was based on the measurement of transmitted electrons through nanodroplets of water.

In nanoclay composites, particularly from montmorillonite, the shape and dimensions of platelets after extrusion process were observed using TEM and wet-STEM. The differences in the size observed between platelets using TEM and STEM techniques were attributed to the preparation by ultramicrotomy and the effect of projection [72]. Thus, in this case, the combination of microscopy techniques revealed the effect of each step of the process.

20.2.2.5 Cryogenic Transmission Electron Microscopy

Cryogenic transmission electron microscopy (Cryo-TEM) or cryogenic high resolution transmission electron microscopy (Cryo-HRTEM) involves the observation of samples of vitrified macromolecules.

Some of the Cryo-TEM and Cryo-HRTEM applications in polymer materials are (i) studies of crystal transformation, for example, the nucleation process and shape of crystals in lamellar crystals of polybutene-1 [74]; (ii) studies of the morphology of several materials, such as polypeptides [75]; investigations on the degradation and erosion of polymers, for example, studies of random copolymers of DTE (desaminotyrosyl-tyrosine ethyl ester) and PEG [76]; and (iv) studies of the spatial structure of polymer brushes, such as poly(styrenesulfonate) chains grafted to core particles of PS latex [77].

The technique is under development. Studies on specimen thickness dependence during cryo-TEM of hydrated soft materials were proposed by Yakovlev et al. [78]. The authors found a way to obtain higher spatial resolution using thin specimens and higher electron doses.

20.2.2.6 High Angle Annular Dark Field (HAADF)-STEM

A high angle detector can be added to STEM to obtain atomic resolution images where the contrast is directly related to the atomic number (Z-contrast image). These images are therefore directly interpretable, in contrast to conventional HRTEM which uses phase contrast and needs simulation for interpretation. HAADF-STEM is an incoherent imaging technique whose characteristics include high signal-to-noise ratio, linearity of the signal intensity, and a reduced number of imaging artifacts. Thus, information on the nanoscale organization of polymeric materials, which is not accessible by CTEM, can be obtained by HAADF-STEM.

There are important advantages of this technique compared to CTEM, such as the possibility to use different values of the camera length in HAADF-STEM imaging to enhance the contrast between crystalline and amorphous compounds through diffraction contrast [79], as well as the use of low convergence angles for imaging HAADF-STEM tomography, which allows to obtain information from micrometer-thick samples [80]. Some of the reported applications are described below.

Loos et al. [12] have explored several polymer systems using HAADF-STEM, such as a rubber blend, a carbon-filled conductive nanocomposite, a functional blend, semicrystalline polyethylene, and template-grown nanotubes (polymer and liquid-crystalline material) [81]. The authors discussed the advantages of HAADF-STEM for the morphology characterization of polymer systems. For carbon-based (carbon black (CB)) functional polymer systems HAADF-STEM can provide high contrast between the CB agglomerates and the polymer matrix, revealing details of the interface and permitting a clear assignment of the phases [79].

Additional reports [82] revealed that the volume concentrations of CB can be precisely determined using HAADF-STEM. In another study, the same authors reported that the filler distribution in polymer nanocomposite systems could be clearly determined [83]. They also observed the nanoscale organization in a photoactive layer of a polymer solar cell that could not be seen with CTEM [79].

Phase separation of poly(vinylidene fluoride) (PVDF) and sulfonated PS within a poly(vinylidene fluoride)-*graft*-poly(styrenesulfonic acid) (PVDF-*g*-PSSA) system and ionic sulfonic aggregates could be determined using HAAFDF-STEM [84].

Finally, significant contrast increase of stained samples was reported when the HAADF-STEM technique was used for several systems, such as cellulose microfibers and whiskers within poly(lactic acid) [85].

20.2.2.7 *Z-Contrast*

Several studies of particle formation using different methods were performed using Z-contrast STEM [86, 87]. Some of the reports involved the study of the dispersion of colloidal CdSe semiconductor nanocrystals embedded in poly[2-methoxy-5-(2-ethyl-hexyloxy)-1,4-phenylene-vinylene] (MEH-PPV) polymer films [88]. In another report, the authors [89] discussed the possibility of measuring absolute thicknesses of atomic columns if the crystal structure was known. In fact, Z-contrast STEM can have a resolution of atomic and subnanometer order. Thus, the technique is able to provide the three-dimensional shape profile reconstructed from the atomic columns. Another application of Z-contrast involved the study at atomic resolution of the structures exhibited by polymer-capped Pt and Pd nanoclusters used as a model of an electrocatalyst [90]. The advantages of subnanometer resolution and the atomic number contrast make it possible to study atomic structures in detail.

Z-contrast has been used to distinguish between two phases using the differences in the atomic number of the particular phase of the analyzed material. Some of the applications reported involved distinguishing a liquid crystal from polymer nanotubes [81].

20.2.2.8 *Low and High Voltage Transmission Electron Microscopy*

Low voltage transmission electron microscopy (LV-TEM) allows to obtain high contrast images of samples from a variety of polymer and organic molecules [91]. LV-TEM has been applied to obtain images of the phase structure of polymer blends without a prior staining procedure [92]. The instrument used in the technique combines light and electron sources (voltage of 5 kV) and charge-coupled device (CCD) imaging. Some of the reported studies are related to the phase structure of polycarbonate/poly(styrene-*co*-acrylonitrile) (PC/SAN), polystyrene/polypropylene (PS/PP), and polyethylene/polypropylene (PE/PP, ADFLEX). The authors have compared the results with LV-STEM at 25 kV. Additional studies have used LV-TEM to identify the morphology of polymers such as PEDOT [93] and polyethylene [91].

Several studies have been carried out in order to understand the relief of ultrathin sectioning and the effect of the imaging at low voltages [94, 95]. The studied polymers involved hard matrixes and soft particles, such as high impact PS, and polymer blends (e.g., PC/SAN blend). From these studies, the authors showed the correspondence between mechanical behavior and morphology of polymers, thus surface relief and phase structure.

In contrast to LV-TEM, studies on the morphology and microdeformation behavior of PP–wood composites modified with high amounts of maleated poly(propylene) as a coupling agent were carried out using high voltage transmission electron microscopy (HV-TEM) [96]; the authors reported the effect of using coupling agents on the adhesion properties between matrix and wood fillers and the resulting increase of the composite's mechanical properties.

20.2.2.9 *Electron Energy-Loss Spectroscopy*

Elemental mapping (EDX) and EELS by EFTEM allows the characterization of interfaces with low spatial resolutions (<10 nm) and high elemental detection sensitivity. EELS, in addition, has the ability to reveal different forms of the same element. Thus, EELS solves important application-oriented problems associated with hetero interfaces, nanoscale mixing, and nanophase separation. Several applications have been reported on the basis of the fact that each polymer has a different EELS fingerprint. Thus, EELS can be a way to differentiate one phase from another. Many studies have been performed in order to improve the information obtained from polymer characterization using EELS. In the following, some research in the field will be briefly described.

Yakovlev and Libera [97] studied the dose-limited imaging of soft materials in STEM as a way of controlling the spatial resolution and avoiding chemical or structural damage. The authors used the low loss of an EELS spectrum to provide a guide to enhance the dose-limited spatial resolution for soft-materials imaging. Also, it has been reported [98] that the spatial resolution is limited by the dose constraints in order to avoid radiation damage. As a consequence, it is necessary to use fine electron probe sizes that reduce counts in the energy-loss spectra.

Libera [99] has presented an alternative for the study of polymer morphology avoiding the staining procedure as a way to induce amplitude contrast. He proposed the use of EELS to study different polymer systems to obtain several levels of resolution (related to the radiation sensitivity of the material) when studying interfaces, such as those in polystyrene–poly(2-vinyl pyridine) homopolymer blends, epoxy–alumina interfaces, and hydrated polymers. Polymers could be distinguished from each other on the basis of the energy-loss spectra in their low loss (valence) and core loss (elemental composition).

A detailed study on the influence of fast secondary electrons from a 200 keV incident electron beam on the characteristic 7 eV π–π* peak in PS was carried out using EELS with STEM. Siangchaew and Libera [100] found a relation between the π-bond degradation, the total radiation

dose, and the dose rate. At higher rates, the π bond was less damaged. Cryo and room temperatures did not affect the damage behavior. The authors concluded that damage to the valence bonds was at least partly due to core excitations.

Regarding applications, nanoscale morphology could be studied in soft materials such as polymers and biological tissue using EELS [101–104].

A combination of cryo-STEM and EELS allowed the study of the spatial distribution of water in frozen hydrated polymers. Because of the reduced information spectra due to the sensitivity of the samples, Sousa et al. [98] reported a method to identify the water in the sample. The problem was studied using theoretical and experimental approaches. They considered hydrophilic poly(vinyl pyrrolidone) (PVP) dispersed in a hydrophobic matrix of PS.

Spatially resolved EELS in STEM was used to examine the size, structure, and composition of material interphases. In particular, the aliphatic bis(*p*-aminocyclohexyl)methane (PACM20) curing agent and the aromatic diglycidyl ether of bisphenol-A (DGEBA) epoxy resin were used in getting spatially resolved $\pi-\pi^*$, carbon, and thickness profiles in the epoxy phase near the interphase area [105].

Polymer composites are being studied by HRTEM, EELS, scanning tunneling spectroscopy (STS), Raman spectroscopy, and allied techniques. In addition, polymer grafting on carbon nanotubes has been studied using EELS. In particular, the covalent attachment of polymer chains onto nanotube surfaces could be successfully proved using low loss EELS [106, 107]. In addition, the propagation of concentric cracks around carbon fibers was observed using EELS, paying special attention to plasmons [108].

An extensive list of applications includes spatial distribution of several elements in a matrix using EELS [108], for example, in a natural rubber [109]; study of the interfaces between a polymer and an adhesive, as in the case of poly(butylene terephthalate) (PBT) and an epoxy adhesive, to correlate the nanoscale interfacial structure with the adhesion strength by EFTEM [110]; characterization of the coating of nanosized particles [111]; studies on the accelerated vulcanization process with regard to the interactions between rubber and ZnO particles [112]; multilayer films of polymers [113]; intercalation of barium atoms in poly(*p*-phenylene) matrixes in atoms per molecules [114]; and studies on the rate and mechanism of hydrolytic degradation and erosion in bioresorbable polymers by EELS and cryo-STEM to determine morphological changes [76].

20.2.2.10 Energy-Filtered Transmission Electron Microscopy EFTEM uses the low electron energy-loss spectroscopy (LEELS) to generate spectral images and enables the search of the spatial distribution of molecules, ions, and particles within nanostructured solids, which could be differentiated by small changes. Thus, as reported, EFTEM provides a molecular map resolution near the bright-field resolution of the same instrument. It is also observed that slight changes in the molecules produce intensity variations in the molecular spectra [115]. Some examples of the application of this technique to polymer materials are described next. Also, there is a review by Ribbe [116] focusing on the advances in EFTEM imaging techniques applied to polymeric materials.

EFTEM by EELS in the image-spectrum mode was used in several applications to polymeric materials such as the following:

1. *In Copolymers and Polymer Blends*. EFTEM was applied to differentiate the phases using the energy transitions due to chemical bondings [117], colloidal dispersions of natural rubber, and styrene-acrylic latex with inorganic particles [118]. The spatial distribution of clay platelets in polymer nanocomposites was investigated using TEM images; nevertheless, this is more difficult than the case of polymer blends. Linares et al. [119] proposed the use of EFTEM crossover region to clearly observe clay nanoplatelets within a polymer blend matrix. The materials studied were natural rubber and poly(styrene-Bu acrylate), poly(styrene-Bu acrylate) and poly(vinyl chloride), as well as natural rubber and starch.

2. *In Polymer-Functionalized Nanoparticles and Nanocomposites*. EFTEM was used to evaluate the covalent bonding of polymer coating on nanoparticles and the nanoparticle dispersion, as in a polycarbonate/alumina nanocomposite [120].

3. *In Polymer–Polymer Interfaces*. EFTEM was used to analyze the effect of annealing temperature on the interfacial structures of copolymers, such as poly(methyl methacrylate)/polystyrene-*co*-polyacrylonitrile (PMMA/SAN) random copolymer [121] and PMMA/SAN random copolymer bilayer films [112]; to study the interface between a polymer and an adhesive, looking for a relationship between the nanoscale interfacial structure and the adhesion strength [110]; and to understand the effect of annealing temperature on the interphase by annealing at different temperatures and using elemental mapping and image-EELS on EFTEM.

4. *Inorganic Polymers*. To study the morphology of polymers [122] and polymer brushes [123].

5. *Conductive Polymers*. EFTEM was used to follow the distribution of ions inside the polymer and the ion-exchange processes as well as to study the elemental distributions in the polymer nanofibers [124], the distribution of lithium ions in solid copolymer electrolytes for lithium batteries [125] and the particle morphology of copolymers [116].

20.3   THREE-DIMENSIONAL MICROSCOPY

20.3.1   Introduction

2D imaging techniques (including optical microscopy, SEM, TEM, and AFM) have been widely used for several decades to study multicomponent polymeric materials (e.g., polymer blends, block copolymers, and polymer composites) [1]. However, 2D micrographs do not fully display the 3D morphological complexity, as they are just cross sections, thin sections, or projections of the bulk specimens. Consequently, qualitative interpretation of 2D images is not always easy. For instance, transversely cut rods can be confused with isolated droplets [126]. When it comes to quantitative assessment of a geometrical parameter, the situation is even more complicated because 2D images generally give only limited pieces of structural information with low statistical accuracy. For some applications, stereological methods (i.e., mathematical relations between 2D and 3D geometrical parameters) can be used to extract 3D information from 2D micrographs [127–130]. However, this approach is limited to a number of geometrical parameters and is contingent on the statistical significance of the micrographs [126, 131].

Scattering techniques (i.e., small angle light, X-ray, or neutron scattering) give statistically averaged structural information of the scattering volume. However, scattering methods do not provide an intuitive morphological insight (i.e., real-space images) as microscopy does. Hence, some knowledge of the morphologies as well as the use of models is usually required to obtain structural parameters. A typical protocol for a complete morphological characterization includes 2D microscopy followed by a hypothesized 3D structure which is tested by scattering measurements. This protocol carries the latent misinterpretation of 2D micrographs, especially for the case of complex interfaces (e.g., bicontinuous structures [126, 132, 133]).

To overcome the above drawbacks, a new technique, namely, 3D microscopy has emerged and rapidly evolved in recent years [132–134]. Obtaining 3D images involves specialized microscopes or attachments (as described below) as well as additional image processing [135] and 3D-rendering algorithms [136]. The reward for this extra equipment and image processing effort is direct 3D information and the computation of parameters not available from any other technique (e.g., local curvature distributions, and local topology).

### 20.3.2   Methods to Obtain 3D Micrographs

There are two ways to generate 3D images: (mechanical or optical) serial sectioning and tomography. Mechanical sectioning has been used to image metal alloys [137–139] and is in principle applicable to polymeric materials. However, this technique is destructive and requires extra steps to align the 2D micrographs [137]. In optical sectioning, a system with a small depth of field (DOF) is used to image a series of sections of the bulk specimen. Optical sectioning has the advantage of filtering the stray scattered light originated from outside the section. This "gating" property allows imaging through moderately low scattering media (e.g., biological tissue or blends of polymers with similar refractive indices). The most popular technique that uses this approach is confocal microscopy (described in the following section). In tomography, a system with a large DOF is used to record projections of the object at different angles. Transmission electron microtomography (TEMT) and X-ray microtomography (μ-CT) have been used to image multiphase polymer-related materials. These techniques are described below.

20.3.2.1   Laser Scanning Confocal Microscopy (LSCM)
In confocal microscopy, the object is illuminated with a focused laser spot, and the light from the object is refocused onto a small pinhole placed in front of the light detector [140, 141]. Images are acquired point by point and reconstructed with a computer algorithm, allowing 3D reconstructions of topologically complex objects. For opaque specimens, this is useful for surface profiling, while for nonopaque specimens interior structures can be imaged. LSCM is a very attractive technique because it does not require time-consuming sample preparation and the image acquisition is fast and nondestructive. However, it has two major drawbacks: one is that at least the first of the phases has to be fluorescent in order to attain a good contrast in the images; and the second is that to image internal structures, the sample has to be transparent in order to provide an adequate DOF [140]. Figure 20.1 shows the basic setup of a confocal microscope. In order to obtain very high intensities, a laser is used to provide the excitation light. The light (blue lines) reflects off a dichroic mirror, which directs it to an assembly of vertically and horizontally scanning mirrors (not shown). These motor-driven mirrors scan the laser across the specimen. The dye in the specimen is excited by the laser light and fluoresces. The fluorescent (green lines) light is descanned by the same mirrors that are used to scan the excitation light from the laser. This light is then passed through the dichroic mirror and is focused onto the pinhole. The light that passes through the pinhole is measured by a photomultiplier. The lateral and axial resolutions in LSCM (r_{xy} and r_z, respectively) are on the order of 1 μm. They can be calculated with $r_{xy} = 0.61\lambda_{exc}/NA$ and $r_{xy}/r_z = 3.28n/NA$, where λ_{exc} is the excitation wavelength, n is the refractive index of the object medium, and NA is the numerical aperture of the objective lens [141]. In confocal microscopy, one can never get a complete image of the specimen because at any instant, only one point is observed. Thus, for visualization,
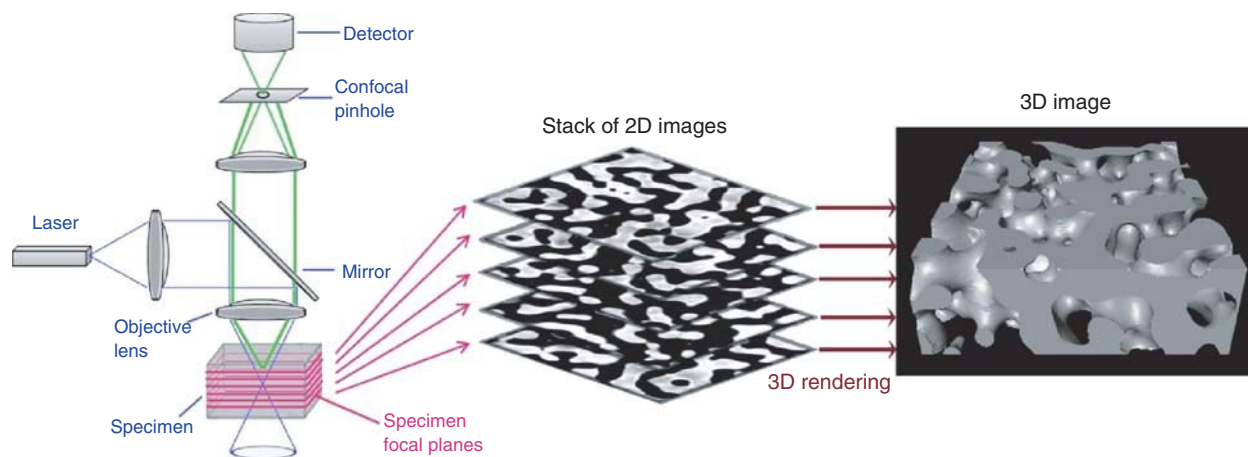
Figure 20.1   Schematic of LSCM. A stack of 2D images is recorded at different focal planes in the specimen and subsequently reconstructed in three dimensions using the marching cubes algorithm [136]. (*See insert for the color representation of the figure*.)

the detector is attached to a computer, which builds up the image one pixel at a time.

Verhoogt et al. pioneered the use of LSCM to visualize polymeric materials [142]. They compared images of the microstructure of the blend made of styrene (ethylene/butylene) styrene (SEBS) block copolymer and poly(ether ester) from LSCM and SEM. Jinnai and coworkers have extensively used LSCM to visualize bicontinuous structures generated during the late stage of spinodal decomposition of binary mixtures of polybutadiene with deuterated polybutadiene [134, 143, 144] and of polybutadiene with poly(styrene-*ran*-butadiene) [134, 145, 146]. Recently, Lopez-Barron and Macosko made 3D images of immiscible polymer blends of polystyrene/styrene-*ran*-acrylonitrile (PS/SAN) copolymer with cocontinuous morphologies during structural coarsening [126, 147–150].

20.3.2.2   X-Ray Microtomography

X-ray μ-CT has similar spatial resolution as LSCM (∼1 μm) but the big advantage is its stronger penetration power. This is particularly useful to image opaque materials. For instance, Montminy and coworkers [151] used a commercial desktop μ-CT to image and analyze 3D structures of polyurethane foams (Fig. 20.2). They developed an image analysis algorithm to measure and quantify the number of struts and windows in the foam structure. However, the main limitation of this technique in pure polymer samples is the poor contrast because of the low X-ray absorption in polymers. Therefore, the use of laboratory X-ray sources allows the imaging of only high contrast samples, including polymer foams [151, 152], biopolymer scaffolds [153], and polymer composites [154–156].

By using a higher X-ray flux (i.e., a synchrotron source), distinct polymer phases can be detected using phase contrast. The interaction of electromagnetic radiation (X-rays) with matter depends on the complex refractive index of matter, $n = 1 - \delta + \beta i$ [134]. The real part δ is associated with phase contrast, which is due to edge-enhancement effects based on diffraction, refraction, and interference, whereas the imaginary part β underlies absorption contrast. Different polymer regions have different refractive indices and thus produce different lateral displacements of a collimated X-ray beam (which is provided by synchrotron X-ray sources). The interference between the transmitted and displaced beams that occurs near the boundary regions of the two polymers gives rise to dark and bright fringes, resulting in edge enhancement. Elmoutaouakkil et al. [157] used synchrotron X-ray μ-CT to analyze the 3D structure of polymer foams. This high X-ray flux enabled quantitative measurements of cell wall thicknesses. Weiss et al. [158] obtained better spatial resolution in bone by using synchrotron X-ray μ-CT. Pyun et al. [159] imaged the cocontinuous structure of a blend of PS and high density polyethylene with X-ray μ-CT. They showed that, as the coarsening proceeded, the specific interfacial area obtained from the analysis of the reconstructed 3D images exceeded that calculated from 2D images, even after applying a stereological correction [126].

20.3.2.3   Transmission Electron Microtomography

TEMT is an emerging technique used for characterization of 3D nanostructures, (e.g., self-assembled block copolymers). The first tomographic reconstructions date from 1968 [160–162]. A large amount of theoretical and technical developments followed these pioneering works. The history, theory, and recent developments in TEMT can be found in two excellent reviews by Jinnai and coworkers [132, 133]. A typical TEMT procedure consists in recording projections at different angles by tilting the specimen with respect to the electron beam in the TEM column. During tilting, misalignments due to

the eccentricity of the specimen stage are unavoidable. Hence, alignment of the digitalized image is necessary before 3D reconstruction. Another problem is the loss of resolution due to the restricted tilt range in TEM, which produces a wedge-shaped region in the Fourier space. This limitation, known as the *missing wedge*, is challenging and is discussed elsewhere [133, 163].

The first report of TEMT on block copolymer nanostructures, by Spontak [164], appeared in 1988. This was followed by three morphological studies carried out in the 1990s [165–167]. Only recently has TEMT become more popular in characterizing polymer nanostructures, including block copolymers [134, 164, 167–173], nanocomposites [174, 175], and polymer nanocomposites [176]. Kawase et al. [177] recently presented a protocol to perform complete rotation (i.e., $90°$) on a ZrO_2/polymer nanocomposite, by which they achieved truly quantitative TEMT for the first time.

This technique has been particularly useful to characterize complex (bicontinuous) nanostructures, for example, gyroid (G) and perforated lamellar (PL). 2D projections of these structures, acquired by regular TEM, give inconclusive identification because they appear identical along several projection axes. For instance, the "wagon wheel" pattern in TEM projections associated with the double Gyroid (DG) formed in triblock copolymers (Fig. 20.2a) [178], was once believed to be a Schuartz D surface with *Pn3_m* symmetry [179]. Small-angle X-ray scattering and self-consistent field theory calculations allowed the correct interpretation of the G surface [180]. However, the first direct observation of the 3D DG was recently achieved by Jinnai and coworkers using TEMT on a poly(styrene-*b*-isoprene-*b*-polystyrene) (SIS) triblock copolymer (Fig. 20.2b) [132, 168]. The authors were also able to compute the local curvature distributions of the gyroid interface (using the methods described in the following section) and use them to infer details of the nanostructure stability in terms of packing constraints.

Studying topological transformations during order–order transitions (OOTs) in block copolymer systems is challenging with CTEM because of the complexity of the interface between the two evolving structures. TEMT is ideal to study these transitions. An example is shown in Figure 20.3, which shows the reconstructed 3D micrograph of poly(styrene-*b*-isoprene) (SI) block copolymer during the OOT from hexagonally packed cylinder (HEX) phase to DG [181]. OOTs between DG and hexagonal PL domains and between single helix to DG were also studied with TEMT [182, 183]. Another complex interface that was experimentally ascertained with TEMT is the lamellar twist grain boundary (in SI block copolymer), in which two lamellar nanodomains intersect forming the Scherk's first surface [145].
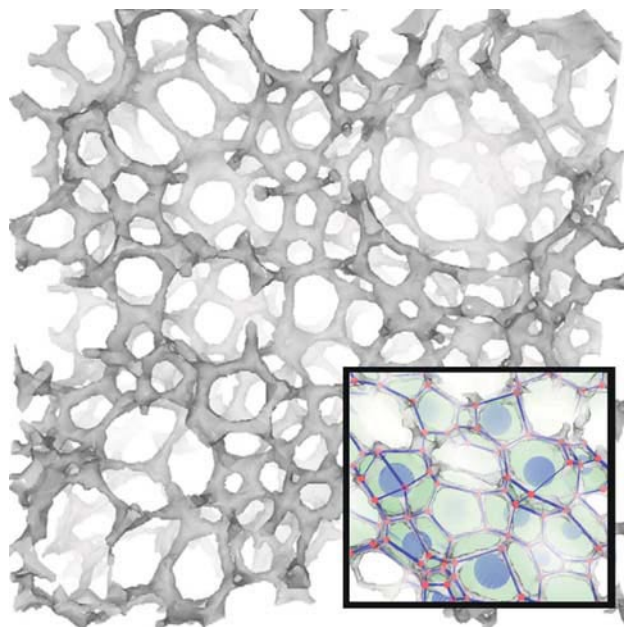

Figure 20.2 3D-rendered image of a polyurethane foam obtained via X-ray μ-CT. The black voxels within this image represent the locations of foam struts, while the white areas represent void space. The inset show a close-up of the foam structure showing the correlation between the detected strut, vertex, and cell locations and the original foam volume. The large blue spheres in the image indicate the centers of detected foam cells. *Source*: Reprinted with permission from Journal of Colloid and Interface Science, Vol. 280, M.D. Montminy, A.R. Tannenbaum, C.W. Macosko, The 3D structure of real polymer foams, Journal of Colloid and Interface Science 2004, 280, pages 202–211 [152]. Copyright 2004 Elsevier. (*See insert for the color representation of the figure.*)

20.3.3 3D Image Analysis

One of the key advantages of 3D images is that they contain rich structural information (not available using any other technique) which can be extracted using cutting-edge quantitative image analysis. Even some basic structural parameters, such as volume fractions or interfacial area per unit volume, can be inaccurately estimated from 2D images. These parameters are directly and easily measured from 3D images. Moreover, 3D microscopy is the only experimental technique capable of evaluating local curvatures, normal vector fields, and genus (interconnectivity) [134, 148, 150]. Some of the methods to evaluate these parameters are summarized below.

Typical 3D reconstruction from 2D sections or projections involves the generation of a triangular mesh describing the interface between the phases via nonstructuring meshing methods based on the marching cubes algorithm [136]. Geometrical parameters are then obtained by applying differential geometry on the mesh. For instance, the interfacial area per unit volume (Q) is simply obtained
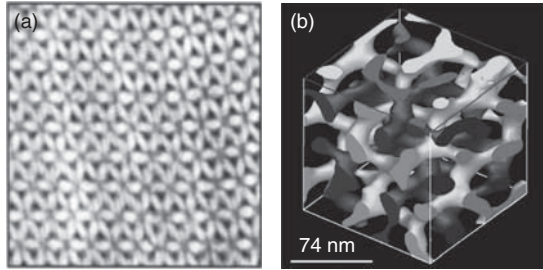
Figure 20.3 (a) TEM projection of a thin section of poly (isoprene-*b*-styrene-*b*-dimethylsiloxane) (ISD) triblock copolymer. The poly(dimethylsiloxane) (D) domains appear dark, while the poly(isoprene) (I) and poly(styrene) (S) domains appear white. The "wagon wheel" pattern is associated with the two D networks arranged in a gyroid morphology. *Source*: Reprinted with permission from Reference [178]. Copyright 1999 American Chemical Society. (b) 3D reconstructed TEMT image of the gyroid morphology in a SIS triblock copolymer. The nonintersecting light and dark channels correspond to the minority styrene microphases, while the majority (isoprene) microphase is transparent. The edge of each cube equals twice the periodic length. *Source*: Reprinted with permission from Jinnai H, Spontak RJ, Nishi T. Transmission Electron Microtomography and Polymer Nanostructures. Macromolecules 2010, 43, 1675–1688 [132]. Copyright 2010 American Chemical Society.

by adding the areas (A_i) of all the triangles in the mesh and dividing by the total volume (V), that is, $Q = \sum_{i=1}^{N} A_i / V$, where N is the total number of triangles.

The shape of the interface can be locally determined by the values of the principal curvatures (κ_1 and κ_2) or alternatively by the values of the mean (H) and the Gaussian (K) curvatures defined as $H = (\kappa_1 + \kappa_2)/2$ and $K = \kappa_1 \cdot \kappa_2$, respectively. H and K are very useful to characterize biphasic systems. H is directly related to the interfacial energy of systems containing an interface; hence it is a measure of the microstructure stability [149, 184, 185]. The Gaussian curvature is particularly useful to characterize the local shape of surfaces. The sign of K gives the type of points on a surface: hyperbolic if $K < 0$, elliptic if $K > 0$, parabolic if $K = 0$ but $H \neq 0$, and planar if $K = H = 0$. Additionally, the area integral of K is directly proportional to the Euler characteristic χ, which is a measure of the surface topology, via the Gauss–Bonnet theorem [186].

Jinnai and coworkers developed two methods to quantify the curvature between the two phases by applying differential geometry to the 3D reconstructed images [149]: (i) using a parallel surface method, they measured the area-average of H [187] and (ii) using a sectioning and fitting (SF) method, they were able to measure the local values of H and K [144]. More recently, Lopez-Barron and Macosko [148] presented a simplified method to calculate the local values of H and K, which was based on a surface patch parameterization algorithm. This method uses the coordinate transformation method proposed by Sander and

Zucker [188]. Figure 20.4a shows the details of a triangular mesh, with the mean curvature of each triangle represented by a color scale map for an immiscible blend of PS and styrene-*ran*-acrylonitrile (SAN) copolymer with cocontinuous morphology [149]. The red- and blue-colored triangles represent regions of high interfacial energy, which supply the driving force for coarsening these structures.

The probability densities of the mean curvature, $P_H(H)$, and the Gaussian curvatures, $P_K(K)$ at different annealing times provide a great deal of information about the dynamics of coarsening of biphasic materials. $P_H(H)$ and $P_K(K)$ for PS/SAN cocontinuous blend are shown in Figure 20.4b [148]. The fact that $P_H(H)$ is symmetric and centered at zero indicates that the area-averaged mean curvature, $\langle H \rangle$, is zero and hence the coarsening progresses along a path of minimal energy. Both distributions narrow down with time, which confirms that the interfacial energy is minimized by minimizing the interfacial curvature. The values of $P_K(K)$ are mostly negative at all times, indicating that the surface is predominantly hyperbolic (i.e., saddle shaped) during the whole coarsening process. Topological transformations of bicontinuous structures can also be determined from the computed values of χ via the area integral of local K, as described elsewhere [148, 189–191].

Interface anisotropy is another important parameter in multiphase fluids. This is mostly relevant to relate rheological properties with microstructure [192]. The interface anisotropy can be quantified using the interface tensor q_{ij}, defined as $q_{ij} = \frac{1}{V} \int_S \left(n_i n_j - \frac{1}{3}\delta_{ij} \right) \, dS$ where n_i is the ith component of the interface unit normal vector, δ_{ij} is the Kronecker delta, and the integration is performed on the surface S contained in the volume V. Hence, the unit normal vector is required in order to compute q_{ij}.

The three components of the normal vector cannot be computed from 2D micrographs without previous knowledge (or assumption) of the interface shape. For simple shapes with axial symmetry that can be described with simple functions, such as ellipsoidal droplets and cylindrical threads, analytical expressions for n_i (and q_{ij}) have been obtained from 2D images [193–195]. However, for complex interfaces (e.g., cocontinuous structures), which are not axisymmetric and cannot be described by any analytical equation, this approach is not applicable.

Recently, Lopez-Barron and Macosko [150] introduced the local cross-product method (LCPM) to compute n_i and q_{ij} from 3D images. The method is applicable to any kind of interface, regardless of its complexity, provided that 3D images are available. The method is based on a simple geometric principle: given a triangular polygon, with vertices, $p_n(x_n, y_n, z_n)$ (with $n = 1, 2, 3$), the normal to that triangle can be obtained by first describing two directional vectors in the same plane, for example, $\mathbf{d}_1 = (x_2 - x_1, y_2 - y_1, z_2 - z_1)$ and $\mathbf{d}_2 = (x_3 - x_2, y_3 - y_2, z_3 - z_2)$ (Fig. 20.5a). The
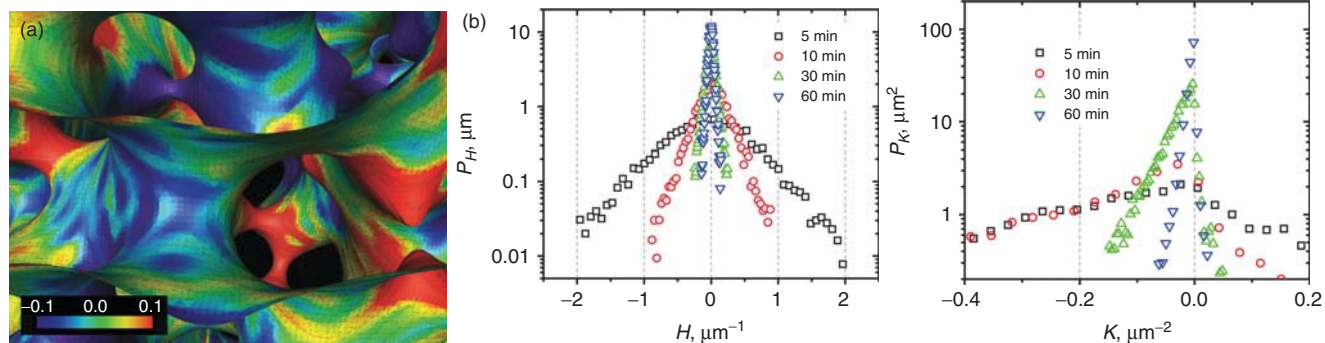
Figure 20.4 (a) 3D-rendered interface of 50/50 PS/SAN cocontinuous blend. The color in each triangle represents the value of the mean curvature given by the color bar scale. *Source*: Reproduced with permission from López-Barrón C, Macosko CW. A new model for the coarsening of cocontinuous morphologies. *Soft Matter* 2010;6:2637–2647 [149]. Copyright 2010 The Royal Society of Chemistry. (b) Probability densities of the mean and the Gaussian curvatures of the 50/50 PS/SAN interface at different annealing times. *Source*: Reprinted with permission from Lopez-Barron C, Macosko CW. Characterizing interface shape evolution in immiscible polymer blends via 3D image analysis. *Langmuir* 2009;25:9392–9404 [148]. Copyright 2009 American Chemical Society. (*See insert for the color representation of the figure*.)
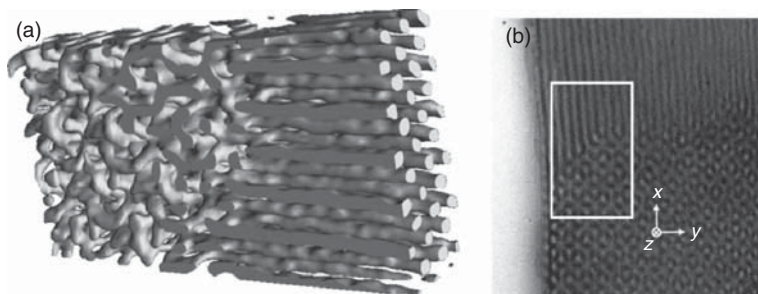

Figure 20.5 (a) 3D reconstructed image of coexisting DG and HEX phases in a SI block copolymer. Only the PS domain is shown. The dimensions of the hexahedron are 400 nm × 200 nm × 80 nm (X, Y, Z). (b) TEM image of the sample region from which the 3D image was reconstructed (boxed area). Here, z is the direction of the incident electron beam and xz is the film plane. *Source*: Reprinted with permission from Park H-W, Jung J, Chang T, Matsunaga K, Jinnai H. New Epitaxial Phase Transition between DG and HEX in PS-*b*-PI. *J. Am. Chem. Soc.* 2009, 131, 46–47 [181]. Copyright 2009 American Chemical Society.

cross product $d_1 \times d_2$ gives a vector perpendicular to the polygon. Therefore, the unit normal vector is given by $n = d_1 \times d_2/|d_1 \times d_2|$. Accordingly, given a surface that can be represented with a triangular mesh, the normal vector field is readily obtainable by performing the cross-product on each triangle in the mesh. Figure 20.5b shows the details of the normal vector field for a cocontinuous interface computed with the LCPM. Lopez-Barron and Macosko tested the LCPM with the gyroid surface, and found good agreement between the anisotropy computed with LCPM and that computed analytically as well as with the predictions from Doi–Ohta's theory [192]. They also applied the method to measure the anisotropy evolution of a cocontinuous PS/SAN blend during uniaxial elongation and subsequent relaxation (Fig. 20.6) [150].

20.3.4 Summary

LSCM, X-ray μ-CT, and TEMT have been progressively evolved into mature techniques to visualize and quantify microstructures of polymer-related materials in three dimensions. These techniques currently allow the accurate evaluation of basic geometrical parameters (such as interfacial area per unit volume) and of more specific parameters (such as local curvatures and normal vector fields). Topology (network connectivity) is also important and achievable with 3D image analysis. Moreover, 3D microscopy is actively branching out into more sophisticated techniques such as four-dimensional microscopy, where a time sequence of x,y,z images is treated as a single object in the x,y,z,t space. Combination of 3D microcopy with other techniques (such as self consistent field theory calculations
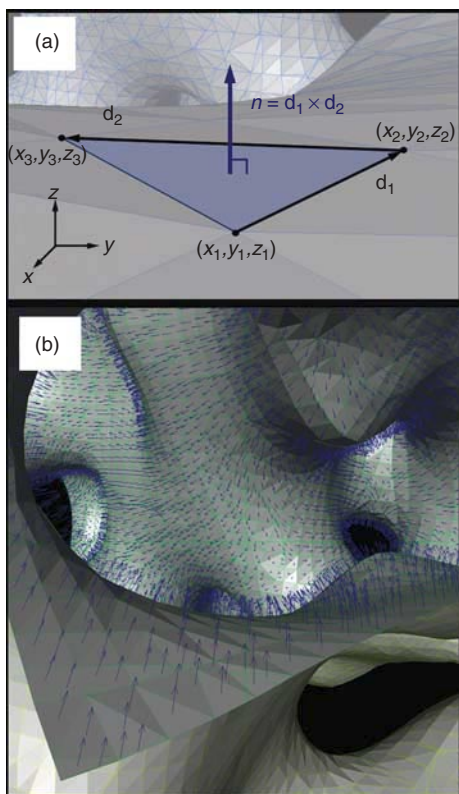
Figure 20.6 (a) Schematic of the computation of the vector normal to a triangle. (b) Detail of the normal vector field generated with the LCPM on a cocontinuous interface. *Source*: Reprinted with permission from López-Barrón CR, Macosko CW. Direct measurement of interface anisotropy of bicontinuous structures via 3D image analysis. *Langmuir* 2010;26 (17):14284–14293 [150]. Copyright 2010 American Chemical Society. (*See insert for the color representation of the figure*.)

[172] and neutron reflectometry [173]) has yielded basic understanding of block copolymer self-assembly from the molecular level or in confined geometries.

REFERENCES

1. Sawyer LC, Grubb DT, Meyers GF. *Polymer Microscopy*. Springer: New York; 2008.

2. Michler GH. *Electron Microscopy of Polymers*. Springer-Verlag Berlin Germany; 2008.

3. Bosco G. Trend Anal Chem: TRAC 2011;30:1189.

4. Drummy LF, Kübel C. Polym Rev 2010;50:231.

5. Buschow, K.H.J, Cahn, Robert, Flemings, Merton, Ilschner, Bernhard, Kramer, Edward, Mahajan, Subhash, Veyssiere, Patrick. *Encyclopedia of materials: Science and Technology*. Elsevier Sci. The Netherlands. 2001. p. 7654.

6. Michler GH. Appl Spectrosc Rev 1993;28:327.

7. Martin DC, Thomas EL. Polymer 1995;36:1743.

8. Kunz M, Shull K. Polymer 1993;34:2427.

9. Libera MR, Egerton RF. Polym Rev 2010;50:321.

10. Bar G, Tocha E, Garcia-Meitin E, Todd C, Blackson J. J Macromol Symp 2009;282:128.

11. Osten EF, Smith MS. Microsc Microanal 1998;4:814.

12. Loos J, Sourty E, Lu K, de With G, Bavel SV. Macro-molecules 2009;42:2581.

13. Berry VK. In: Gupta RK, Kennel E, Kim K-J, editors. *Polymer Nanocomposites Handbook*. CRC Press. FL, USA. Eds: R. K. Gupta, E. Kennel, K.-J. Kim. USA. 2010. p 309.

14. Zhang F, Liu J, Huang H, Du B, He T. Eur Phys J E Soft Matter 2002;8:289.

15. He L, Xu Q, Song R, Hua C. Polym Compos 2010;31:913.

16. Aprahamian I, Mendes P, Leung KC-F, Benitez D, Stoddart JF. The functionalization of polymers with gold nanoparticles using reversible supramolecular self-assembly processes. Abstracts of Papers In: 232nd ACS National Meeting; 2006 Sept 10–14; San Francisco (CA).

17. Brinkmann M, Rannou P. Macromolecules 2009;42:1125.

18. Tonomura A. *Electron Holography*. Springer; New York, USA. 1942.

19. Cowley JM. Ultramicroscopy 1992;41:335.

20. Gabor D. Nature 1948;161(4098):777–778.

21. Haine ME, Mulvey T. J Opt Soc Am A 1952:42. pp. 763–769.

22. Simon P, Lichte H, Wahl R, Mertig M, Pompe W. BBA – Biomembranes 2004;1663:178.

23. McCartney MR, Agarwal N, Chung S, Cullen DA, Han M-G, He K, Li L, Wang H, Zhou L, Smith DJ. Ultramicroscopy 2010;110:375.

24. Lichte H, Reibold M, Brand K, Lehmann M. Ultramicroscopy 2002;93:199.

25. Barton KE, Boettcher SH, Gaudiello JG, Kimball LJ, Wang YYF. US Patent. US Patent Number 7560692. 2008.

26. Chou T-M, Libera M, Gauthier M. Polymer 2003;44:3037.

27. Lawrence JR, O'Neill FT, Sheridan JT. Optik – Int J Light Electron Opt 2001;112:449.

28. García C, Fimia A, Pascual I. Optik – Int J Light Electron Opt 2002;113:111–116.

29. Gölzhäusera A, Völkela B, Grunzea M, Kreuzer HJ. Micron 2002;33:241.

30. Binh VT, Semet V, Garcia N. Ultramicroscopy 1995;58. p. 307.

31. Crozier PA, *In situ* nanoscale observation of polymer structures with electron microscopy. Abstracts of Papers In: 224th ACS National Meeting; 2002 Aug 18–22; Boston (MA).

32. Erts D, Lõhmus A, Lõhmus R, Olin H. Appl Phys A Mater Sci Process 2001;72. pp. S71–S74.

33. Nafari A, Ghavanini FA, Bring M, Svensson K, Enoksson P. J Micromech Microeng 2007;17:2102.

34. Jiang N, Gao S, Wei XL, Liang XL, Chen Q. J Phys Chem C 2008;112:15631.

35. Nafari A, Karlen D, Rusu C, Svensson K, Olin H, Enoksson P. J Microelectromech Syst 2008;17. p. 328.

36. Golberg D, Costa PMFJ, Mitomea M, Bandoa Y. J Mater Chem 2009;19:909.

37. Golberg D, Costa PMFJ, Lourie O, Mitome M, Bai X, Kurashima K, Zhi C, Tang C, Bando Y. Nano Lett 2007;7:2146.

38. Lu Y, Huang JY, Chao Wang SSaJL. Nat Nanotechnol 2010;5. p. 218–224.

39. Nafari A, Angenete J, Svensson K, Sanz-Velasco A, Enoksson P. J Micromech Microeng 2010;20. pp. 064017.

40. Crozier PA, Oleshko VP, Westwood AD, Cantrell RD. *In situ* environmental transmission electron microscopy of gas phase Ziegler-Natta catalytic polymerization of propylene. Presented at Institute of Physics Conference Series; 2001.

41. Tatsuya K, Yoshiyuki A. Effect of long-chain branching on mechanical strength of polyethylenes. In: KEK Proceedings; 2002.

42. Bucknall CB. J Microsc 2001;201:221.

43. Garcia Gutierrez MC, Henning S, Michler GH. J Macromol Sci Phys 2003;B42:95.

44. Michler GH. J Macromol Sci Phys 2001;B40:277.

45. Michler GH, Bucknall CB. Plast Rubber Compos 2001;30:110.

46. Qian D, Dickey EC, Andrews R, Rantell T. Appl Phys Lett 2000;76:2868.

47. Qian D, Dickey EC. J Microsc 2001;204:39.

48. Kim GM, Michler GH, Poetschke P. Polymer 2005;46:7346.

49. Kim G-M, Lach R, Michler GH, Chang Y-W. Macromol Rapid Commun 2005;26:728.

50. Mitchell GR, Holt JJ, Thornley SA, Chai CK. X-ray and neutron scattering rheology: Crystallization from sheared melts. Abstracts of Papers. In: 222nd ACS National Meeting; 2001 Aug 26–30; Chicago (IL).

51. Castillo J, Dimaki M, Svendsen WE. Integr Biol 2009;1:30.

52. Stokes DJ, Morrissey F, Lich BH. J Phys Conf Ser 2005;26:50.

53. Yusof NLBM, Lim LY, Khor E. Adv Chitin Sci 2003;7:7.

54. Wei Z, Gourevich I, Field L, Coombs N, Kumacheva E. Macromolecules 2006;39:2441.

55. Tajima A, Higuchi T, Yabu H, Shimomura M. Colloids Surf A Physicochem Eng Asp 2008;313,314:332.

56. Higuchi T, Yabu H, Shimomura M. J Nanosci Nanotechnol 2007;7:856.

57. Zhou NC, Chan CD, Winey KI. Macromolecules 2008;41:6134.

58. Rueckert B, Kolb U. Micron 2005;36:247.

59. Faucheu J, Chazeau L, Gauthier C, Cavaille J-Y, Goikoetxea M, Minari R, Asua JM. Langmuir 2009;25:10251.

60. Gao C, Li W, Jin YZ, Kong H. Nanotechnology 2006;17:2882.

61. Vesely D, Ronca G. J Microsc 2001;201:137.

62. Madbouly SA, Otaigbe JU, Hassan MK, Mauritz KA. PMSE Preprints 2006;94:831.

63. Jeremic D, Cooper P, Brodersen PH. Holzforschung 2007;61(3):272.

64. Yokoyama N, Nonaka Y, Kurata T, Sakai S, Takahashi S, Kasemura T. J Appl Polym Sci 2007;104:1702.

65. Ding S-Y, Rumbles G, Jones M, Tucker MP, Nedeljkovic J, Simon MN, Wall JS, Himmel ME. Macromol Mater Eng 2004;289:622.

66. Xie S, Zhang S, Wang F, Yang M, Seguela R, Lefebvre J-M. Compos Sci Technol 2007;67:2334.

67. Taubert A, Wind JD, Paul DR, Koros WJ, Winey KI. Polymer 1881;2003:44.

68. Benetatos NM, Winey KI. J Polym Sci B Polym Phys 2005;43:3549.

69. Gai PL. Microsc Microanal 2002;8:21.

70. Bogner A, Thollet G, Basset D, Jouneau P-H, Gauthier C. Ultramicroscopy 2005;104:290.

71. Bogner A, Guimaraes A, Guimaraes RCO, Santos AM, Thollet G, Jouneau PH, Gauthier C. Colloid Polym Sci 2008;286:1049.

72. Vermogen A, Masenelli-Varlot K, Vigier G, Sixou B, Thollet G, Duchet-Rumeau J. J Nanosci Nanotechnol 2007;7:3160.

73. Barkay Z. Appl Phys Lett 2010;96:183109/1.

74. Tosaka M, Kamijo T, Tsuji M, Kohjiya S, Ogawa T, Isoda S, Kobayashi T. Macromolecules 2000;33:9666.

75. Pakstis LM, Ozbas B, Hales KD, Nowak AP, Deming TJ, Pochan D. Biomacromolecules 2004;5:312.

76. Sousa A, Schut J, Kohn J, Libera M. Macromolecules 2006;39:7306.

77. Wittemann A, Drechsler M, Talmon Y, Ballauff M. J Am Chem Soc 2005;127:9688.

78. Yakovlev S, Misra M, Shi S, Libera M. J Microsc 2009;236:174.

79. Sourty E, van Bavel S, Lu K, Guerra R, Bar G, Loos J. Microsc Microanal 2009;15:251.

80. Kangbo L, Erwan S, Joachim L. J Electron Microsc 2010;59:S39.

81. Schaper AK, Kurata H, Yoshioka T, Masaki T. Microsc Microanal 2007;13:336.

82. Lu K, Erwan S, Joachim L. J Electron Microsc 2010;59:S39.

83. Lu K, Sourty E, Guerra R, Bar G, Loos J. Macromolecules 2010;43:1444.

84. Huang HS, Chen CY, Lo SC, Lin CJ, Chen SJ, Lin LJ. Appl Surf Sci 2006;253:2685.

85. Tanem BS, Kvien I, van Helvoort ATJ, Oksman K. ACS Sym Ser – Cell Nanocompos 2006;938:48.

86. Vaughn JM, Gao X, Yacaman M-J, Johnston KP, Williams RO 3rd., Eur J Pharm Biopharm 2005;60:81.

87. Reyes-Reyes M, Lopez-Sandoval R, Arenas-Alatorre J, Garibay-Alonso R, Carroll DL, Lastras-Martinez A. Thin Solid Films 2007;516:52.

88. Kadavanich AV, Kippeny TC, Erwin MM, Pennycook SJ, Rosenthal SJ. J Phys Chem B 2001;105:361.

89. Kadavanich AV, Kippeny T, Erwin M, Rosenthal SJ, Pennycook SJ. Nanocrystal thickness information from Z-STEM: 3-D imaging in one shot. Presented at Materials Research Society Symposium Proceedings; 2001.

90. Sanchez SI, Small MW. J.-m. G. Nuzzo. J Am Chem Soc 2009;131:8683.

91. Martin DC, Drummy LF, Coufalova E. Mater Res Soc Sym Proc – Adv Biomater: Characterization, Tissue Eng Compl 2002;711:107.

92. Lednicky F, Coufalova E, Hromadkova J, Delong A, Kolarik V. Polymer 2000;41:4909.

93. Martin DC, Wu J, Shaw CM, King Z, Spanninga SA, Richardson-Burns S, Hendricks J, Yang J. Polym Rev 2010;50:340.

94. Lednicky F, Pientka Z, Hromadkova J. J Macromol Sci Phy 2003;B42:1039.

95. Lednicky F, Hromadkova J, Pientka Z. Polymer 2001;42:4329.

96. Hristov V, Krumova M, Michler G. Macromol Mater Eng 2006;291:677.

97. Yakovlev S, Libera M. Micron 2008;39:734.

98. Sousa A, Aitouchen A, Libera M. Ultramicroscopy 2006:106:130–145.

99. M. R. Libera, Imaging unstained polymer morphology using electron energy-loss spectroscopy. Abstracts of Papers. In: 224th ACS National Meeting; 2002 Aug 18–22; Boston (MA).

100. Siangchaew K, Libera M. Philos Mag A: Phys Condens Matter: Struct, Defects Mech Properties 2000;80:1001.

101. Francoise W, Genevieve V, Jaafar G, Patricia G, Jean-Claude P. Biology of the cell / under the auspices of the European Cell Biology Organization 2002;94:55.

102. Sung-Hee P, Seong-Geun O, Ji-Young M, Sung-Sik H. Colloids Surf B Biointerfaces 2005;44:117.

103. Sousa A, Sengonul M, Latour R, Kohn J, Matthew L. Langmuir 2006;22:6286.

104. Bockelmann U, Lunsdorf H, Szewzyk U. Environ Microbiol 2007;9:2137.

105. Arayasantiparb D, McKnight S, Libera M. J Adhes Sci Technol 2001:15:1463–1484.

106. Dehonor M, Masenelli-Varlot K, Gonzalez-Montiel A, Gauthier C, Cavaille J-Y, Terrones M. J Nanosci Nanotechnol 2007;7:3450.

107. Chiang LY, Anandakathir R, Hauck TS, Lee L, Canteenwala T, Padmawar PA, Pritzker K, Bruno FF, Samuelson LA. Nanoscale 2010;2:535.

108. Reznik B, Fotouhi M. Compos Sci Technol 2008;68:1131.

109. Rippel MM, Leite CAP, Galembeck F. Anal Chem 2002;74:2541.

110. Horiuchi S, Hamanaka T, Aoki T, Miyakawa T, Narita R, Wakabayashi H. J Electron Microsc 2003;52:255.

111. Shen Y, Gokhale A, Wei D, Dave R, Pfeffer R. Coating of ultra-fine particles using supercritical fluids. In: AIChE Spring National Meeting, Conference Proceedings; 2006 Apr 23–27; Orlando (FL).

112. Horiuchi S, Dohi H. Langmuir 2006;22:4607.

113. Chernev B, Belegratis MR, Ingolic E. Macromol Symp–Modern Polym Spectrosc 2008;265:272.

114. Dubois M, Dailly A, Ghanbaja J, Merlin A, Billaud D. Polymer 2002;44:801.

115. Linares EM, Leite CAP, Valadares LF, Silva CA, Rezende CA, Galembeck F. Anal Chem 2009;81:2317.

116. Ribbe AE. Recent Res Dev Macromol 2003;7:171.

117. Varlot K, Martin JM, Quet C. Polymer 2000;41:4599.

118. Fonseca VL, Fabio d C B, Aparecida d S C, Paula LCA, Fernando G. J Colloid Interface Sci 2007;309:140.

119. Linares EM, Rippel MM, Galembeck F. ACS Appl Mater Interfaces 2010;2:3648.

120. Chandra A, Turng L-S, Gopalan P, Rowell RM, Gong S. Compos Sci Technol 2008;68:768.

121. Horiuchi S, Yin D, Ougizawa T. Macromol Chem Phys 2005;206:725.

122. Trabelsi S, Janke A, Haessler R, Zafeiropoulos NE, Fornasieri G, Bocchini S, Rozes L, Stamm M, Gerard J-F, Sanchez C. Macromolecules 2005;38:6068.

123. Horiuchi S, Hanada T, Ebisawa M, Yasuhiro M, Kobayashi M, Takahara A. ACS Nano 2009;3:1297.

124. Rubino S, Razaq A, Nyholm L, Stromme M, Leifer K, Mihranyan A. J Phys Chem B 2010;114:13644.

125. Gomez ED, Panday A, Feng EH, Chen V, Stone GM, Minor AM, Kisielowski C, Downing KH, Borodin O, Smith GD. Nano Lett 2009;9:1212.

126. López-Barrón CR, Macosko CW. J Microsc 2010;242:242.

127. Miles RE. J Microsc 1981;121:21–27.

128. Russ JC. *Practical Stereology*. New York: Plenum Press; 1986.

129. Howard V, Reed MG. *Unbiased Stereology: Three-Dimensional Measurement in Microscopy*. Oxford, New York: Scientific Publishers/Springer; 1998.

130. Underwood EE. *Quantitative Stereology*. Reading (MA): Addison-Wesley Pub. Co; 1970.

131. Exner HE. Image Anal Stereol 2004;23:73–82.

132. Jinnai H, Spontak RJ, Nishi T. Macromolecules 2010;43:1675.

133. Jinnai H, Spontak RJ. Polymer 2009;50:1067–1087.

134. Jinnai H, Nishikawa Y, Ikehara T, Nishi T. Adv Polym Sci 2004;170:115–167.

135. Russ JC. *The Image Processing Handbook*. CRC Press; 2007. Boca Raton, FL

136. Lorensen WE, Cline HE. SIGGRAPH Comput Graph 1987;21:163–169.

137. Alkemper J, Voorhees PW. J Microsc 2001;201:388–384.

138. Alkemper J, Voorhees PW. Acta Mater 2001;49:897–902.

139. Wilson JR, Kobsiriphat W, Mendoza R, Chen H, Hiller JM, Miller DJ, Thornton K, Voorhees PW, Adler SB, Barnett SA. Nat Mater 2006;5:541.

140. Sheppard C, Shotton D. *Confocal Laser Scanning Microscopy*. Oxford, New York: Springer; 1997.

141. Inoue S. In: Pawley JB, editor. *Handbook of Biological Confocal Microscopy*. New York: Springer; 2006.

142. Verhoogt H, Van Dam J, Posthuma de Boer A, Draaijer A, Houpt PM. Polymer 1993:34.

143. Jinnai H, Nishikawa Y, Hashimoto T. Phys Rev E 1999;59:R2554.

144. Nishikawa Y, Koga T, Hashimoto T, Jinnai H. Langmuir 2001;17:3254.

145. Jinnai H, Nishikawa Y, Koga T, Hashimoto T. Macromolecules 1995;28:4782.

146. Jinnai H, Koga T, Nishikawa Y, Hashimoto T, Hyde ST. Phys Rev Lett 1997;78:2248–2251.

147. Lopez-Barron CR, Macosko CW. Macromol Symp 2009;283–284:348.

148. Lopez-Barron C, Macosko CW. Langmuir 2009;25:9392.

149. López-Barrón C, Macosko CW. Soft Matter 2010;6:2637.

150. López-Barrón CR, Macosko CW. Langmuir 2010;26:14284.

151. Montminy MD, Tannenbaum AR, Macosko CW. J Colloid Interface Sci 2004;280:202.

152. B. E. Pangerle, N. P. Hammer, M. L. Bidault, R. E. Listemann, R. E. Stevens, X. D. Zhang, C. W. Macosko, In: Proc. Soc. Plast. Ind. Polyurethanes; 1998; Dallas (TX).

153. Donath T, Beckmann F, Heijkants RGJC, Brunke O, Schreyer A. Proc SPIE Int Soc Opt Eng 2004;5535:775.

154. Conner WC, Webb SW, Spanne P, Jones KW. Macromolecules 1990;23:4742.

155. Schilling PJ, Karedla BR, Tatiparthi AK, Verges MA, Herrington PD. Compos Sci Technol 2005;65:2071–2078.

156. Schell JSU, Renggli M, van Lenthe GH, Müller R, Ermanni P. Compos Sci Technol 2006;66:2016.

157. Elmoutaouakkil A, Fuchs G, Bergounhon P, Peres R, Peyrin F. J Phys D: Appl Phys 2003;36:A37.

158. Weiss P, Obadia L, Magne D, Bourges X, Rau C, Weitkamp T, Khairoun I, Bouler JM, Chappard D, Gauthier O, Daculsi G. Biomaterials 2003;24:4591.

159. Pyun A, Bell JR, Won KH, Weon BM, Seol SK, Je JH, Macosko CW. Macromolecules 2007;40:2029.

160. Hoppe W, Langer R, Knesch G, Poppe C. Naturwissenschaften 1968;55:333.

161. De Rosier DJ, Klug A. Nature 1968;217:130.

162. Hart RG. Science 1968;159:1464.

163. Bates RHT, McDonnell MJ. *Image Restoration and Reconstruction*. Oxford, Oxfordshire; New York: Oxford University Press; 1986.

164. Spontak RJ, Williams MC, Agard DA. Polymer 1988;29:387.

165. Spontak RJ, Fung JC, Braunfeld MB, Sedat JW, Agard DA, Kane L, Smith SD, Satkowski MM, Ashraf A, Hajduk DA, Gruner SM. Macromolecules 1996;29:4494.

166. Laurer JH, Hajduk DA, Fung JC, Sedat JW, Smith SD, Gruner SM, Agard DA, Spontak RJ. Macromolecules 1997;30:3938.

167. Radzilowski LH, Carragher BO, Stupp SI. Macromolecules 1997;30:2110.

168. Jinnai H, Nishikawa Y, Spontak RJ, Smith SD, Agard DA, Hashimoto T. Phys Rev Lett 2000;84:518.

169. Yamauchi K, Takahashi K, Hasegawa H, Iatrou H, Hadjichristidis N, Kaneko T, Nishikawa Y, Jinnai H, Matsui T, Nishioka H, Shimizu M, Furukawa H. Macromolecules 2003;36:6962.

170. Wilder EA, Braunfeld MB, Jinnai H, Hall CK, Agard DA, Spontak RJ. J Phys Chem B 2003;107:11633.

171. Dobriyal P, Xiang H, Kazuyuki M, Chen J, Jinnai H, Russell TP. Macromolecules 2009;42:9082.

172. Morita H, Kawakatsu T, Doi M, Nishi T, Jinnai H. Macromolecules 2008;41:4845.

173. Niihara K, Matsuwaki U, Torikai N, Atarashi H, Tanaka K, Jinnai HA. Macromolecules 2007;40:6940.

174. Nishioka H, Niihara K, Kaneko T, Yamanaka J, Nishikawa Y, Inoue T, Nishi T, Jinnai H. Compos Interface 2006;13:589.

175. Zhao Y, Thorkelsson K, Mastroianni AJ, Schilling T, Luther JM, Rancatore BJ, Matsunaga K, Jinnai H, Wu Y, Poulsen D, Frechet JMJ, Paul Alivisatos A, Xu T. Nat Mater 2009;8:979.

176. Jinnai H, Shinbori Y, Kitaoka T, Akutagawa K, Mashita N, Nishi T. Macromolecules 2007;40:6758.

177. Kawase N, Kato M, Nishioka H, Jinnai H. Ultramicroscopy 2007;107:8.

178. Shefelbine TA, Vigild ME, Matsen MW, Hajduk DA, Hillmyer MA, Cussler EL, Bates FS. J Am Chem Soc 1999:121.

179. Thomas EL, Alward DB, Kinning DJ, Martin DC, Handlin DL, Fetters LJ. Macromolecules 1986;19:2197.

180. Hajduk DA, Harper PE, Gruner SM, Honeker CC, Thomas EL, Fetters LJA. Macromolecules 1995;28:2570.

181. Park H-W, Jung J, Chang T, Matsunaga K, Jinnai H. J Am Chem Soc 2009;131:46.

182. Jung J, Park H, Lee S, Lee H, Chang T, Matsunaga K, Jinnai H. ACS Nano 2010;4:3109.

183. Chen C, Hsueh H, Chiang Y, Ho R, Akasaka S, Hasegawa H. Macromolecules 2010;43:8637.

184. Helfrich W. Z Naturforsch C Biosci 1973;28:693.

185. Scholten E, Sagis LMC, van der Linden E. J Phys Chem B 2004;108:12164.

186. Gray A, Abbena E, Salamon S. *Modern Differential Geometry of Curves and Surfaces with Mathematica*. Boca Raton: Chapman & Hall, CRC; 2006.

187. Nishikawa Y, Jinnai H, Koga T, Hashimoto T, Hyde ST. Langmuir 1998;14:1242.

188. Sander PT, Zucker SW, Tracing surfaces for surfacing traces. In: Proceedings of the 1st International Conference on Computer Vision; 1987; London.

189. Jinnai H, Kajihara T, Watashiba H, Nishikawa Y, Spontak RJ. Phys Rev E 2001;64:010803.

190. Jinnai H, Kajihara T, Watashiba H, Nishikawa Y, Spontak RJ. Phys Rev E 2001;64:069903/1.

191. Jinnai H, Watashiba H, Kajihara T, Takahashi M. J Chem Phys 2003;119:7554.

192. Doi M, Ohta T. J Chem Phys 1991;95:1242.

193. Vinckier I, Mewis J, Moldenaers P. Rheol Acta 1997;36:513.

194. Wetzel ED, Tucker CL III, Int J Multiphase Flow 1999;25:35.

195. Almusallam AS, Larson RG, Solomon MJ. J Nonnewton Fluid Mech 2003;113:29.